Ultrasonics - Sonochemistry 70 (2021) 105301

Contents lists available at ScienceDirect

Ultrasonics - Sonochemistry

journal homepage: www.elsevier.com/locate/ultson

Ice nucleation of water droplet containing solid particles under weak ultrasonic vibration

Shaolei Gai, Zhengbiao Peng*, Behdad Moghtaderi, Jianglong Yu, Elham Doroodchi*

Discipline of Chemical Engineering, The University of Newcastle, Callaghan, NSW 2308, Australia

ARTICLE INFO

Keywords:
Micro-sized water droplet
Ice nucleation
Ultrasonic vibration
Cavitation bubble
LBM

ABSTRACT

Water with small volume (a few microlitres or less) often maintains its liquid state even at temperatures much lower than 0 °C. In this study, we examine the onset of ice nucleation in micro-sized water droplets with immersed solid particles under weak ultrasonic vibrations. The experimental results show that ice nucleation inside the water droplets can be successfully induced at relatively high temperatures. The experimental observations indicate that the nucleation sites are commonly encountered in the region between the particle and the substrate. A numerical study is conducted to gain insight into the possible underlying phenomenon for ice nucleation in such systems. The simulation results show that the collapse of cavitation bubbles in the crevice at the particle surface is structure sensitive with the hemisphere-shape crevice generating pressures as high as 1.63 GPa, which is theoretically suitable for inducing ice nucleation.

1. Background

Ice particles have been used as an efficient cold energy storage medium in a number of industrial processes [1,2] due to its large latent heat. In recent years, efforts have been directed mainly towards generating ice particles from micro-sized water droplets to enhance the ice particle quality in terms of size and size distribution, surface smoothness and sphericity [1–5]. However, ice nucleation in micro-sized water droplets proves challenging [6], often requiring a supercooling greater than 30 °C. Such a low operating temperature in water droplet freezing processes is undesirable as it results in a low coefficient of performance (COP) of the refrigeration system.

A variety of methods have been developed for increasing the ice nucleation onset temperature in water droplets, including the addition of freezing catalysts [7,8], application of electro/magnetic fields [9–11] and stimulation by cavitation bubbles [12]. The electro/magnetic fields based nucleation techniques, however, are still in the stage of lab investigation, requiring the deep understanding of the nucleation mechanism [13]. One commonly used active technique for triggering ice nucleation is based on the addition of freezing catalysts having crystal structures similar to ice (ice-like) [14–17], e.g. silver iodide [18]. However, it is still challenging to achieve a relatively high nucleation onset temperature close to 0 °C in small droplets. For instance, Stan et al. [17] investigated the ice nucleation in droplets of 77 μm with AgI nanoparticles, and found none of the droplets froze at temperatures higher than −9.9 °C.

Another approach for reducing the supercooling degree for ice nucleation is the application of power ultrasound. Under the irradiation of power ultrasound waves (frequency: 20 – 100 kHz; intensity > 1 W/cm^2) [19], cavitation bubbles are generated through the alternating cycles of low and high pressures (rarefaction and compression) and have been reported to induce nucleation of water at a relatively high temperature. Hickling [20–22] explained the ultrasonically induced nucleation based on the pressure pulse generated from the collapse of ultrasonic cavitation bubbles which could reach up to 10 GPa [23,24], thus increasing the equilibrium freezing temperature of water and leading to a large supercooling (10–50 °C) [25]. Such advantage endowed by the local high pressure could render a nucleation onset temperature close to 0 °C [23,26].

Since the seminal work of Hickling , several other mechanisms (e.g. bubble oscillation [27–30], molecular segregation [31,32] and negative pressure [33,34]) have been hypothesized as the stimulus for ice nucleation particularly in medium other than water (e.g., sucrose solution [29], fat blends [35] and agar gel [19]). However, the study is still a long way from reaching a consensus on the exact mechanism that triggers ice nucleation, even for a given medium under the specific circumstance. It is worth mentioning that Zhang et al. [30] examined ice nucleation in two types of water samples: i) filtered deionised water and ii) supersaturated deionised water (by mechanically adding in air bubbles). Microstreaming (or flow streams) generated by bubble

* Corresponding authors.
E-mail addresses: zhengbiao.peng@newcastle.edu.au (Z. Peng), elham.doroodchi@newcastle.edu.au (E. Doroodchi).

https://doi.org/10.1016/j.ultsonch.2020.105301
Received 27 May 2020; Received in revised form 30 July 2020; Accepted 30 July 2020
Available online 03 August 2020
1350-4177/

oscillation was captured by Particle Image Velocimetry (PIV) in both water samples, but its effect on ice nucleation was only found in the sample of supersaturated deionised water. In the sample of filtered deionised water, which is the focus of the present study, there was no time lag between the onset of ultrasonic irradiation and the onset of ice nucleation, indicating the occurrence of ice nucleation could mainly follow the Hickling's mechanism.

For micro-sized water droplets, however, ice nucleation by the ultrasonic cavitation method are scarcely reported. This is because cavitation in water droplets is expected to be difficult, due to the lack of impurities (e.g., pre-existing bubbles or hydrophobic particles [36]) contained in such small water droplets. The smaller the water droplet, the less the impurities and the higher the water tensile strength [36]. One may resort to increasing the vibration intensity; however, at such high driving pressures the water droplets may break up in the form of atomisation [37]. A new approach is therefore needed to fully taking advantage of ultrasonic cavitation.

Here we propose using rough micro-sized glass bead particles coupled with a weak ultrasonic vibration. In this method, fine particles are injected into water droplets placed on the surface of a vibrating substrate. It is believed that the rough surface of glass bead particles increases the likelihood of trapping nano-air bubbles within its numerous crevices which in turn may act as cavitation inception sites and be responsible for the onset of ice nucleation under the effect of ultrasonic vibration. In this study, the term "crevice" refers to the tiny space amongst the micro-asperities at the particle surface that could potentially trap nano-air bubbles. Considering the small scale, it is beyond the reach of the experimental approach to obtain data associated with cavitation bubble dynamics inside the crevices. Therefore, the numerical approach becomes a powerful and useful tool for solving such problems at the small scale. Compared to traditional CFD methods [38,39], LBM can deal with the mesoscopic fluid-fluid or fluid-solid interactions more conveniently [40–42]. LBM also has advantages of simplicity, high computational efficiency, and suitability for parallel computing.

In this work, the coupled effect of weak ultrasonic vibration and immersed glass bead particles on the ice nucleation of micro-sized water droplets is investigated experimentally. Specifically, effects of droplet temperature, particle size and concentration on the ice nucleation rate are investigated. To gain insight into the possible underlying phenomenon for ice nucleation triggered in such systems, a numerical study using a pseudo-potential lattice Boltzmann method (LBM) is conducted with the focus placed on cavitation bubble dynamics inside the crevice. The effect of crevice shape, namely square-shape, cone-shape, and hemisphere-shape, on the final collapse pressure is examined with the aim of quantitatively evaluating the Hickling's mechanism.

2. Experiments

The design of experimental setup is based on an earlier study on water droplet ice nucleation by Olmo [43]. Fig. 1 shows the experimental setup which consists of (i) a sonicator (Branson Sonifier 450, Branson Ultrasonics, USA: 400 W, 20 kHz), (ii) a cooling module (MULTICOMP, MCPK2-15828NC-S, UK), (iii) a thermocouple, and (iv) a camera. The sonicator probe was positioned vertically against the left end of the substrate (a steel sheet) with dimensions of 0.1 cm in height, 8 cm in width and 2 cm in depth. The ultrasonic vibration is transferred through the substrate to the right end where water droplets are located. The ultrasonic driving pressure corresponding to a specific sonicator output power was measured by a needle hydrophone system (Precision Ultrasonics, 4.0 mm Needle hydrophone, UK). The top surface of the substrate at the right end was coated with a hydrophobic layer (BOPP, Young's modulus: 1.7 − 2.5 GPa) to maintain the hemispherical shape of the droplet. Water droplets with an equivalent diameter of 800 μm were generated using a 0.5 μL syringe. Glass bead particles (Cospheric, USA) were selected and injected into the droplet (WD-1) using a wet syringe needle. The cooling module was placed underneath the right end of the steel substrate with the temperature precisely controlled by adjusting the input voltage and current. A K-type thermocouple (application range: −75 °C to 250 °C) was placed on the substrate surface close to water droplets for monitoring the operating temperature (T_o). As the micro-sized water droplet is in direct contact with the substrate surface, T_o can be viewed as the droplet temperature. For each run, a reference droplet (WD-2) with no glass bead particles (henceforth called particle) was placed aside. The movement of particles and the freezing behaviour inside WD-1 were captured using a digital microscope camera (RS Pro Wifi Microscope, RS Pro, AU) and a high-speed microscope (Meros, Dolomite, UK). The influence of natural convection between droplets and air on droplet freezing is minimised by a sealed enclosure. In addition, the chamber was purged with nitrogen gas to minimise condensation of water vapour on the substrate and any potential contamination from dusts suspended in the air.

Particles with diameters (D_p) in four size groups (GB1: 63 − 75 μm, GB2: 90 − 150 μm, GB3: 180 − 250 μm and GB4: 250 − 300 μm) were used in present experiments. SEM images (Fig. 2) show that particles have the rough surface with asperities less than 10 μm in diameter (equivalent diameter). As exemplified in Fig. 2(b), a large number of small crevices could exist amongst these asperities. As a consequence, nano-air bubbles are highly likely to be trapped inside the crevices when injected into the water droplet. Also, impurities attached on the surface are likely to be brought into water droplets. Therefore, prior to experiments, all particles were washed in distilled water and stored in a drying oven. To numerically investigate the trapped-bubble collapse dynamics, the structures of the crevice are simplified into three basic shapes: square, cone, and hemisphere, as illustrated in Fig. 3.

During the vibration expansion process, trapped bubbles could work as cavitation inception sites. However, the magnitude of the pressure in between the vibrating substrate and particle is not high enough for growing and detaching cavitation bubbles from the crevice, which often requires a pressure amplitude around − 6 MPa [44,45]. After a certain number of rarefaction and compression cycles, these trapped bubbles reach the maximum size and are likely to collapse given the relatively high pressure built up during the collision between the particle and substrate. For simplicity, we assume the maximum bubble has the similar size to the crevice, as shown in white colour in Fig. 3.

To exclude the influence of possible cavitation inception in the droplet (not in the crevice), the ultrasonic driving pressure in this study is set to be much lower than 0.12 MPa [46]. Applied sonication properties used in this study are listed in Table 1.

For each experiment, the duty cycle of the sonicator was set at 10%, and the output power was changed between 10% to 15%. Further, effects of particle size and number concentration on the ice nucleation onset temperature were examined. A sample population of 40 water droplets under each condition were measured and the number of frozen droplets (N_{drop}) were optically determined. The fraction of frozen droplets is thus defined as $f_{ice} = \frac{N_{drop}}{40}$. A range of benchmark experiments was performed where the individual effects of vibration field (intensities up to 0.0031 W/cm^2) and the presence of particles on the freezing of water droplets (800 μm) were examined separately at $T_o = -9$ °C. The lower limit $T_o = -9$ °C was set to avoid the interference from condensation.

3. Numerical modelling

3.1. Pseudo-potential LBM model

The evolution equation of the pseudo-potential LBM model is expressed as [47]

$$f_\alpha(\mathbf{x} + \boldsymbol{e}_\alpha \delta_t, t + \delta_t) = f_\alpha(\mathbf{x}, t) - \frac{1}{\tau_v}(f_\alpha(\mathbf{x}, t) - f_\alpha^{eq}(\mathbf{x}, t)) + F_\alpha^* \quad (1)$$

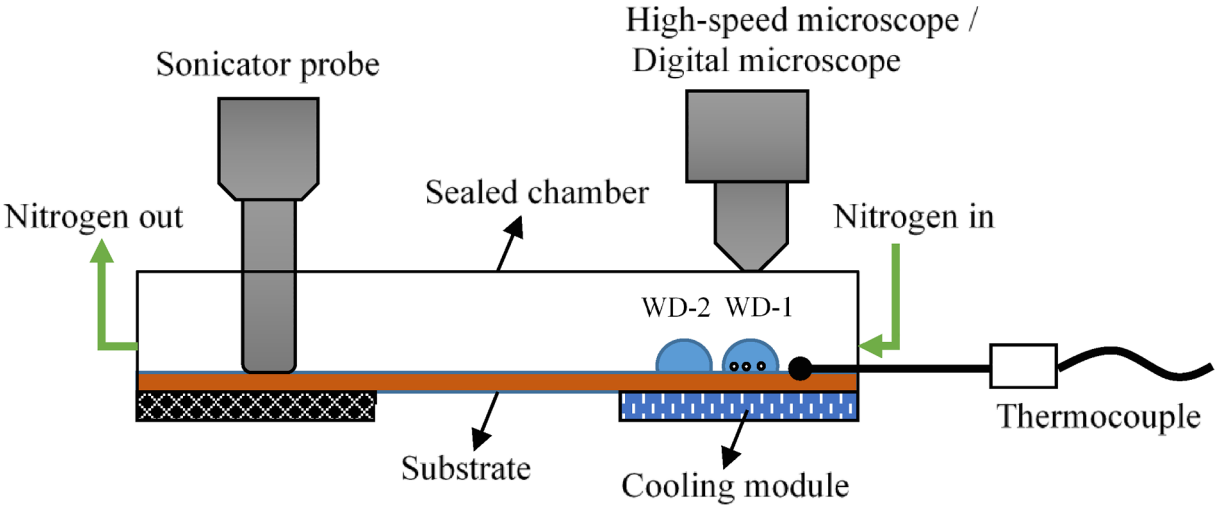

Fig. 1. Schematic of the experimental setup. [WD-1 is water droplet with particles and WD-2 is the reference droplet without any particles].

where f_α is the density distribution function, δ_t is the time step, e_α is the discrete velocity along the αth direction, f_α^{eq} is the equilibrium distribution function, and F_α^* is the forcing term. For D2Q9 (two dimensional and nine velocity scheme) [41], e_α is given as

$$\boldsymbol{e}_\alpha = \begin{bmatrix} 0 & 1 & 0 & -1 & 0 & 1 & -1 & -1 & 1 \\ 0 & 0 & 1 & 0 & -1 & 1 & 1 & -1 & -1 \end{bmatrix} \tag{2}$$

The relaxation time τ_v in relation to the kinematic viscosity ν and is given by

$$\nu = c_s^2\left(\frac{1}{\tau_v} + 0.5\right) \tag{3}$$

where $c_s = \frac{1}{\sqrt{3}}$ is the lattice sound velocity.

The equilibrium density distribution function f_α^{eq} is given by

$$f_\alpha^{eq} = \omega_\alpha \rho\left(1 + \frac{\boldsymbol{e}_\alpha \cdot \boldsymbol{\upsilon}}{c_s^2} + \frac{(\boldsymbol{e}_\alpha \cdot \boldsymbol{\upsilon})}{2c_s^4} - \frac{\boldsymbol{\upsilon}^2}{2c_s^2}\right) \tag{4}$$

where the weighting coefficient ω_α are 4/9 for $\alpha = 0$, 1/9 for $\alpha = 1, 2, 3, 4$ and 1/36 for $\alpha = 5, 6, 7, 8$. The macroscopic velocity $\boldsymbol{\upsilon}$ is calculated by

$$\rho\boldsymbol{\upsilon} = \sum_\alpha \boldsymbol{e}_\alpha f_\alpha + \frac{\delta t}{2}\boldsymbol{F} \tag{5}$$

The forcing scheme proposed by Li et al. [47] is adopted for the forcing term F_α^* in Eq. (1). Li's forcing scheme can be written as

$$S = \omega_\alpha\left(I - \frac{1}{2\tau_v}\right)\left(\frac{\boldsymbol{e}_\alpha - \hat{\boldsymbol{\nu}}}{c_s^2} + \frac{\boldsymbol{e}_\alpha + \hat{\boldsymbol{\nu}}}{c_s^4}\right)\cdot\boldsymbol{F} \tag{6}$$

in which $\hat{\boldsymbol{\nu}}$ is defined as $\hat{\boldsymbol{\nu}} = \boldsymbol{\nu} + \sigma\boldsymbol{F}/\tau_v\psi^2$. The parameter σ is applied to adjust the pseudo-potential model to satisfy the thermodynamic consistency, improve the numerical stability, and achieve a large density ratio. $\boldsymbol{F}$ is the total force acting on the system, including the fluid–fluid interactive force $\boldsymbol{F}_{ff}$, fluid–solid interactive force $\boldsymbol{F}_{fs}$, and the body force $\boldsymbol{F}_b$. For the pseudo-potential LBM model, $\boldsymbol{F}_{ff}$ is given as

$$\boldsymbol{F}_{ff} = -G_{ff}\psi(\mathbf{x})\sum_\alpha^N \omega'(|\boldsymbol{e}_\alpha|^2)\psi(\mathbf{x} + \boldsymbol{e}_\alpha)\boldsymbol{e}_\alpha \tag{7}$$

where $G_{ff} = -1$ is the interaction strength and the weight coefficient $\omega'(|\boldsymbol{e}_\alpha|^2)$ are $\omega'(1) = \frac{1}{13}$ and $\omega'(2) = \frac{1}{12}$. When investigating bubbles in the crevice, the adhesive force $\boldsymbol{F}_{fs}$ between the fluid and the solid boundary needs to be incorporated. $\boldsymbol{F}_{fs}$ is given by

$$\boldsymbol{F}_{fs} = -G_{fs}\psi(\mathbf{x})\sum_\alpha^N \omega_\alpha s(\mathbf{x} + \boldsymbol{e}_\alpha)\boldsymbol{e}_\alpha \tag{8}$$

where $s(\mathbf{x} + \boldsymbol{e}_\alpha)$ is the indicator function, 1 for solid particle and 0 for fluid particle. G_{fs} is the interaction strength and is set to be $G_{fs} = -2.5$ [48] to maintain a hydrophilic surface. The body force $\boldsymbol{F}_b$, i.e., the gravitational force, is neglected.

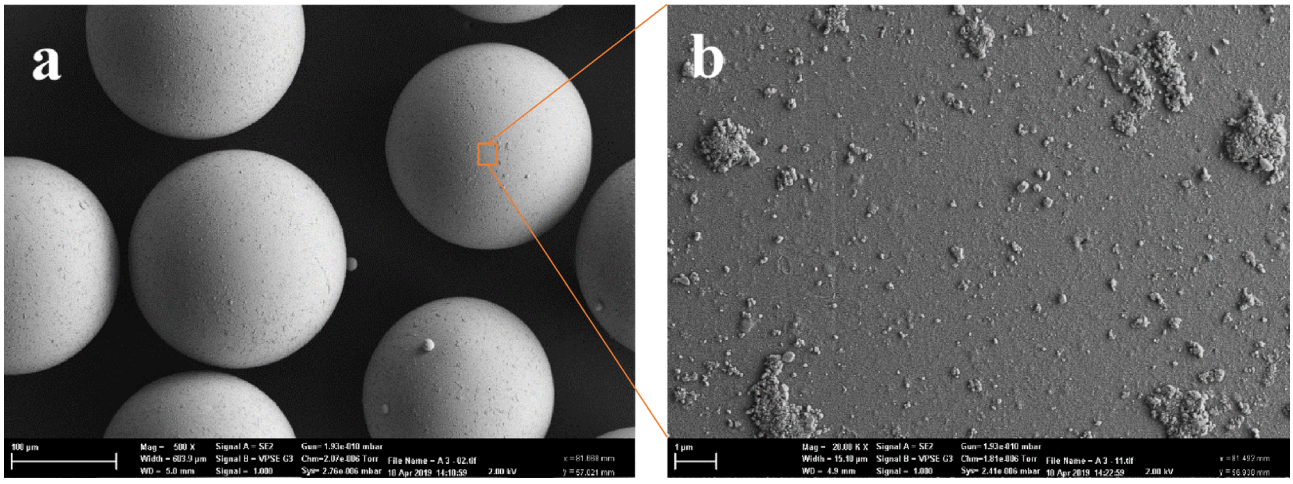

Fig. 2. SEM images of particles: (a) scaled at 100 μm and (b) scaled at 1 μm. [D_p: 180 – 250 μm].

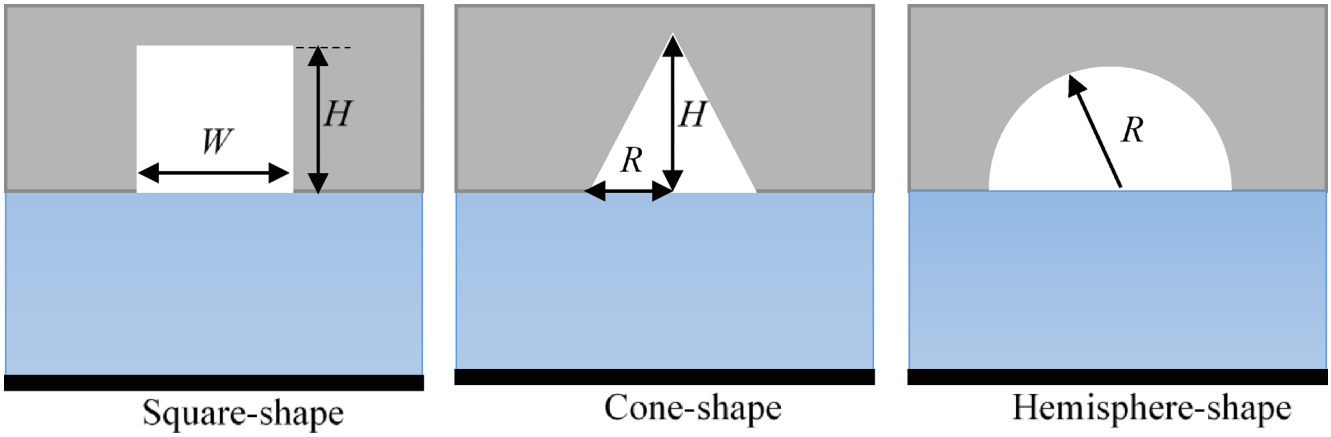

Fig. 3. Simplified basic structures of the asperity crevice on the rough particle surface. [Grey colour represents the body of the particle; light blue colour represents the liquid film; black colour represents the solid substrate].

Table 1
Applied driving pressure varying against the sonicator power output.

Sonicator power output (%)	Driving pressure (MPa)	Vibration intensity (W/cm^2)
10	0.0056 ± 0.00131	0.0011 ± 0.0003
13	0.00825 ± 0.00125	0.0023 ± 0.0003
15	0.00944 ± 0.0011	0.0031 ± 0.0004

$\psi(\boldsymbol{x})$ is the interparticle potential and is given by

$$\psi(\boldsymbol{x}) = \sqrt{2(P_{\mathrm{EOS}} - \rho c_s^2)/G} \tag{9}$$

in which is the equation of state for nonideal fluid. In this study, the Carnahan-Starling (CS) EOS is adopted, which reads

$$P_{\mathrm{EOS}} = \rho RT\frac{1 + b\rho/4 + (b\rho/4)^2 - (b\rho/4)^3}{(1 - b\rho/4)^3} - a\rho^2 \tag{10}$$

where $a = 0.4963(RT_c)^2/P_c$ and $b = 0.18727RT_c/P_c$ with T_c and P_c are the critical temperature and pressure, respectively. We set $a = 0.5$, $b = 4$ and $R = 1$ in this study. The corresponding critical density is given by $P_c = 0.13045$.

3.2. Ice nucleation onset temperature under pressure

Near the wall of a cavitation bubble, water might be subjected to an ultra-high pressure of about 10×10^9 Pa [23,24]. Under such high pressures, the water melting temperature varies dramatically. In this study, the Simon-Glatzel equation [49] is used to describe the ice melting curve as a function of pressure

$$T_m = T_0\left(\frac{\Delta P}{a^*} + 1\right)^{1/b^*} - 273.15 \tag{11}$$

where $\Delta P = (22.06P_{\mathrm{EOS}}/P_c - P_0)$. P_0 and T_0 are the reference pressure and temperature, respectively. The values of P_0, T_0, a^* and b^* for different ice phases are listed in Table 2.

However, the homogeneous ice nucleation onset temperature (T_{hom}, Celsius degree) under high pressures are still absent in the public domain. Hence, the ice nucleation temperature in this study is simplified as [50]

$$T_{\mathrm{hom}} = 0.86T_0\left(\frac{\Delta P}{a^*} + 1\right)^{\frac{1}{b^*}} - 273.15 \tag{12}$$

Table 2
Simon-Glatzel equation parameters for the melting curve of ices [49].

Ice form	Triple point	P_0 (MPa)	T_0 (K)	a^* (MPa)	b^*
Ih	Gas-Ih-liq	6.11657×10^{-4}	273.15	− 414.5	8.38
III	Ih-III-liq	209.5	251.15	101.1	42.86
V	III-V-liq	335.0	256.43	373.6	8.66
VI	V-VI-liq	618.4	272.73	661.4	4.69

3.3. Model validation

To verify the thermodynamic consistency, the grid size of a gravity-free computational domain is set as 201×201 lattices. The periodic boundary scheme is applied to all four boundaries. The initial density of liquid is set as $\rho_l = 0.2$. Note that, for the simulation results of LBM, the unit of time t is 'ts', the unit of length L is 'lu', and the unit of density ρ is 'mu/lu^3'. The temperature is dimensionless. To induce phase transition, an extremely small density perturbation of $10^{-8}\rho_l$ is placed on the horizontal symmetric line of the computational domain at $t = 0$. Fig. 4 shows the density coexistence curve by the present LBM model. The left curve is the vapour branch, and the right curve is the liquid branch. Clearly, the simulation results by the present model have a good agreement with the Maxwell theoretical results.

To further confirm the validity of the developed model, a single free bubble with an initial radius of $R_0 = 40$ in an infinite area is simulated

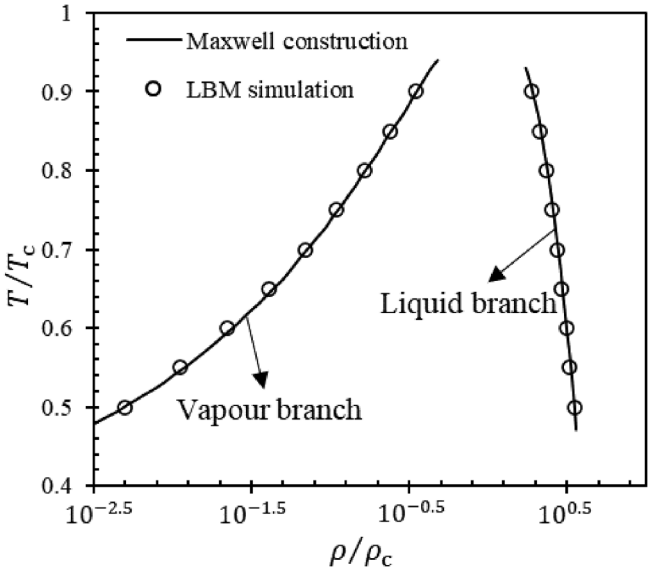

Fig. 4. Comparison of the MRT-LBM model coexistence curve with the Maxwell construction.

and compared against the analytical solutions. Here we set the computational domain as401 × 401 lattices. The initial vapour pressure is set as $\rho_v = 0.0095$ at $T = 0.7T_c$. The non-equilibrium extrapolation boundary scheme [51,52] is applied to the four boundaries. To induce cavitation bubble growth and shrinkage, the initial liquid density is artificially changed to obtain a proper pressure difference $\Delta P = P_l - P_v$. Under a critical $\Delta P = \Delta P_{cri}$, the bubble radius will remain unchanged. In other words, for a given initial bubble, if $\Delta P > \Delta P_{cri}$, the vapour bubble will start shrinking rather than cavitating as condensation is preferable in terms of lowering the system free energy. On the contrary, if $\Delta P < \Delta P_{cri}$, cavitating will dominate the bubble size evolution process. The density field of the computational domain is initialized by

$$\rho(x,y) = \frac{\rho_l + \rho_v}{2} + \frac{\rho_l - \rho_v}{2}\left\{\tanh\left[\frac{2\sqrt{(x-x_0)^2 + (y-\lambda r_0)^2} - R_0}{W}\right]\right\} \tag{13}$$

The analytical solution for the bubble size evolution can be obtained by the Rayleigh-Plesset (R-P) equation. For a two dimensional simulation, R-P equation is boundary sensitive [53]. Therefore, following [40,53], the revised R-P equation is written as

$$\ln\left(\frac{R_{bound}}{R}\right)\rho_l\left(R\ddot{R} + \frac{3}{2}\dot{R}^2\right) + 2\eta_l\frac{\dot{R}}{R} + \frac{\theta}{R} = P_b - P_{bound} \tag{14}$$

where R_{bound} is the computational domain size, P_b is the bubble pressure, and P_{bound} is the pressure at the boundary. The revised R-P equation is solved using the 4th order Runger-Kutta integration algorithm. For the comparison between the analytical solution and the simulation results, the lattice values are used for all the variables in the R-P equation. The viscosity can then be given as $\eta_l = (2\tau_v - 1)/6$. The surface tension $\theta = 0.0191$ is obtained by the Laplace law [40]. The comparison between the analytical solution and the simulation results is shown in Fig. 5. Clearly, the simulation results have very good agreements with the revised R-P equation solutions. The critical pressure for $R_0 = 40$ is $\Delta P_{cri} = -4.8 \times 10^{-4}$. As predicted by revised the R-P equation, the bubble grows with $\Delta P > \Delta P_{cri}$, and shrinks with $\Delta P < \Delta P_{cri}$.

4. Results and discussion

Results of the benchmark experiments on the nucleation of 800 μm droplets using only the ultrasonic vibration field or particles showed no occurrence of ice nucleation. Specifically, when particles were injected into the water droplet without imposing the vibration field, the liquid state was maintained for over 5 min at $T_o = -9$ °C, suggesting that impurities brought into the water droplet by particles have a marginal effect on water droplet ice nucleation. Similar results were obtained when the vibration field was applied solely with intensities up to 0.0031 W/cm^2 and $T_o = -9$ °C. The study is then extended to examine the coupled effect of the vibration field and the presence of solid particles on ice nucleation of water droplet under the same operating conditions.

Fig. 6 shows the ice nucleation evolution process under the coupled effect with the vibration intensity of 0.0011 W/cm^2 and $T_o = -5$ °C. Clearly, even under such weak ultrasonic vibrations, the ice nucleation can be successfully induced with the assistance of particles. Fig. 6(a) shows a typical evolution of ice nucleation and the freezing process within an 800 μm water droplet containing particles under the effect of ultrasonic vibration field. Prior to the onset of ice nucleation, particles move randomly in the water droplet. For each particle, the momentum is transferred from the vibrating substrate and its neighbouring particles. Under strong particle–particle and particle–substrate interactions, the ice nucleation is induced in the water droplet. The ice nucleation is seen starting from a single particle and spread rapidly through the entire supercooled space at a speed of ~0.8 cm/s. In addition, for all nucleation cases, the nucleation sites are constantly found to lie in the region between a particle and the substrate. This might suggest that the particle–substrate interaction is the main cause of ice nucleation. If the ice nucleation is triggered by the particle–particle interaction, ice should be found growing from the gap of two contact particles. However, this phenomenon was not observed in experiments.

To reveal the behaviour of ice nucleation induced by particle–substrate interaction, T_o is increased further to −2 °C to slow down the ice growth rate and increase the chance of observing the initial stage of the ice nucleus. As shown in Fig. 6(b), one tiny six-fold symmetrical snowflake ice crystal (around 50 μm) is formed. This snowflake indicates that the ice originates from a point ice nucleus. This point ice nucleus could be generated from the direct interaction between the substrate and the particle, or from the cavitation bubbles in the crevice [19,25,28,29,31,32,34,54,55].

In order to understand how the particle–substrate interaction affects the water droplet ice nucleation, effects of key parameters including droplet temperature, particle number concentration and size on the ice nucleation behaviour are examined. The effects of vibration intensity and induction time on the droplet freezing rate have been reported in our earlier work [56].

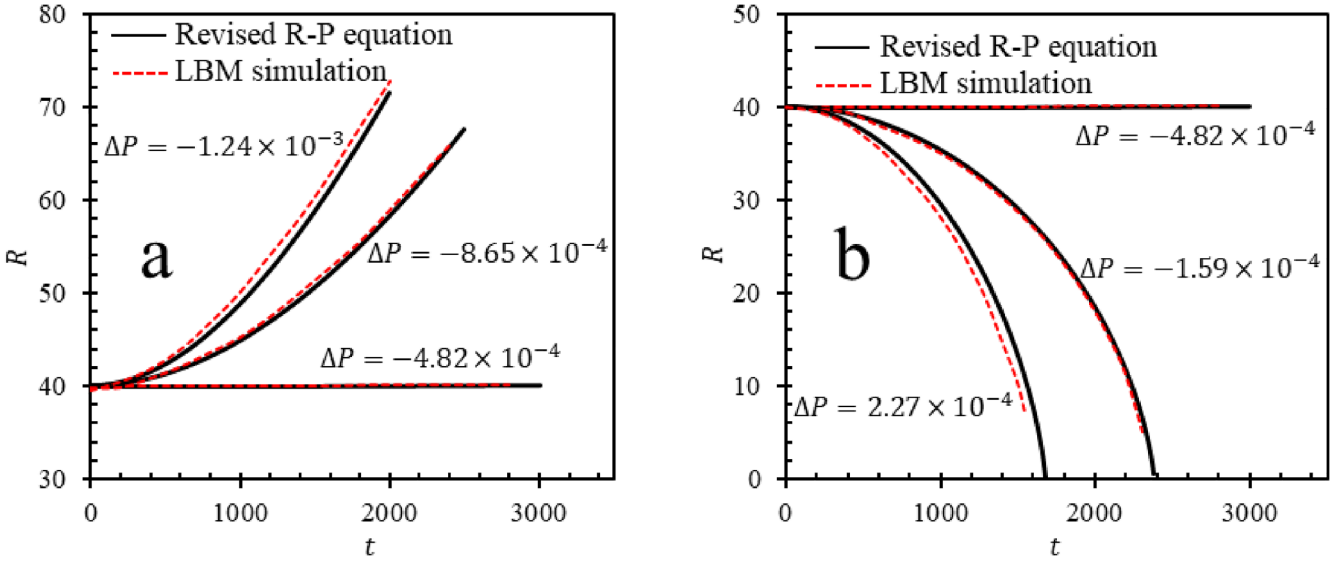

Fig. 5. Comparison of the cavitation bubble size evolution between the simulation results and the analytical solution. (a) bubble growth; (b) bubble collapse.

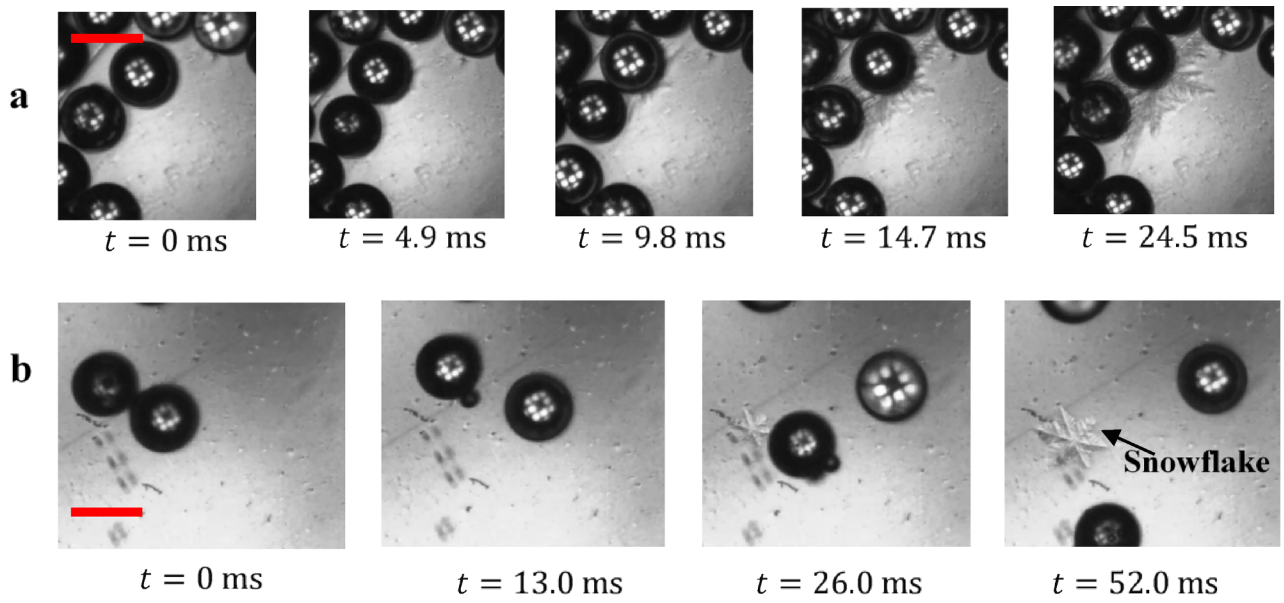

Fig. 6. Ice nucleation evolution process under the coupled effect of the ultrasonic vibration field and particles. (a) $T_o = -5$ °C, particle (D_p: 90 – 150 μm) number concentration: 5 – 10 particles/droplet; (b) $T_o = -2$ °C, particle (D_p: 90 – 150 μm) number concentration: 3 particles/droplet. Scale bar: 100 μm.

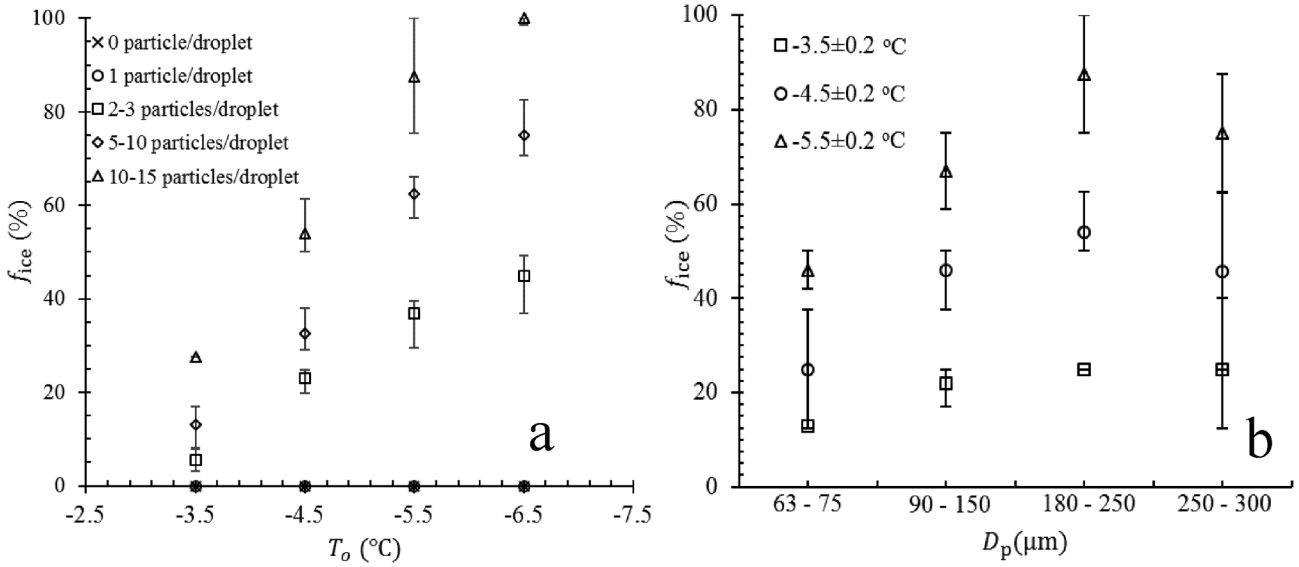

Fig. 7. Fraction of the frozen droplets over temperature, particle number concentration and size. (a) vibration intensity: 0.0011 W/cm^2, droplet size: 0.8 mm, vibration induction time: 10 s, and D_p: 180 – 250 μm; (b) vibration intensity of 0.0011 W/cm^2, vibration induction time: 10 s, particle number concentration: 10–15 particles/droplet, droplet size: 0.8 mm.

Fig. 7(a) shows the variation of f_{ice} as a function of T_o at the ultrasonic vibration intensity of 0.0011 W/cm^2 for different particle number concentrations. It can be seen that f_{ice} increases significantly, doubles in value, as the particle number concentration in the water droplet increases from 2 – 3 to 10 – 15 particles per droplet. Also, as the particle number concentration decreases, lower freezing temperatures are required to maintain the same f_{ice}. It is noteworthy the combined effect on f_{ice} becomes significant only when there are more than one particle inside the water droplet. Water droplets containing one or no particle remain unfrozen even with T_o as low as −6.5 °C. Fig. 7(b) shows the nucleation rate of a supercooled water droplet as a function of particle sizes. As the particle size increases, f_{ice} increases first and drops at D_p = 180 – 250 μm. This phenomenon is more pronounced with reducing the droplet temperature.

SEM images of GB1– GB4 particles show that the asperities are densely distributed on the particle surface, as shown in Fig. 8. During the strong collision between particles and the vibrating substrate, water film between them is highly squeezed leading to the surge of local pressure. The force balance between the gravitational force and the substrate inertial force is assumed in the water film. Accordingly, the direct collision pressure (P_d) generated by a single asperity in the collision could be simplified as

$$P_d = \frac{4m_g\left(\frac{2\pi f R_v}{\rho c} + g\right)}{\pi D_a^2} \tag{15}$$

The first term in the bracket of Eq. (15) is the substrate acceleration amplitude based on the vibration intensity [12]. In Eq. (15) m_g is the particle mass; f is the ultrasonic vibration frequency; ρ is the water density; c is the local sound speed; g is the gravitational acceleration; P_v is the absolute value of the maximum driving pressure from the substrate (as listed in Table 1); and D_a is the equivalent diameter of the

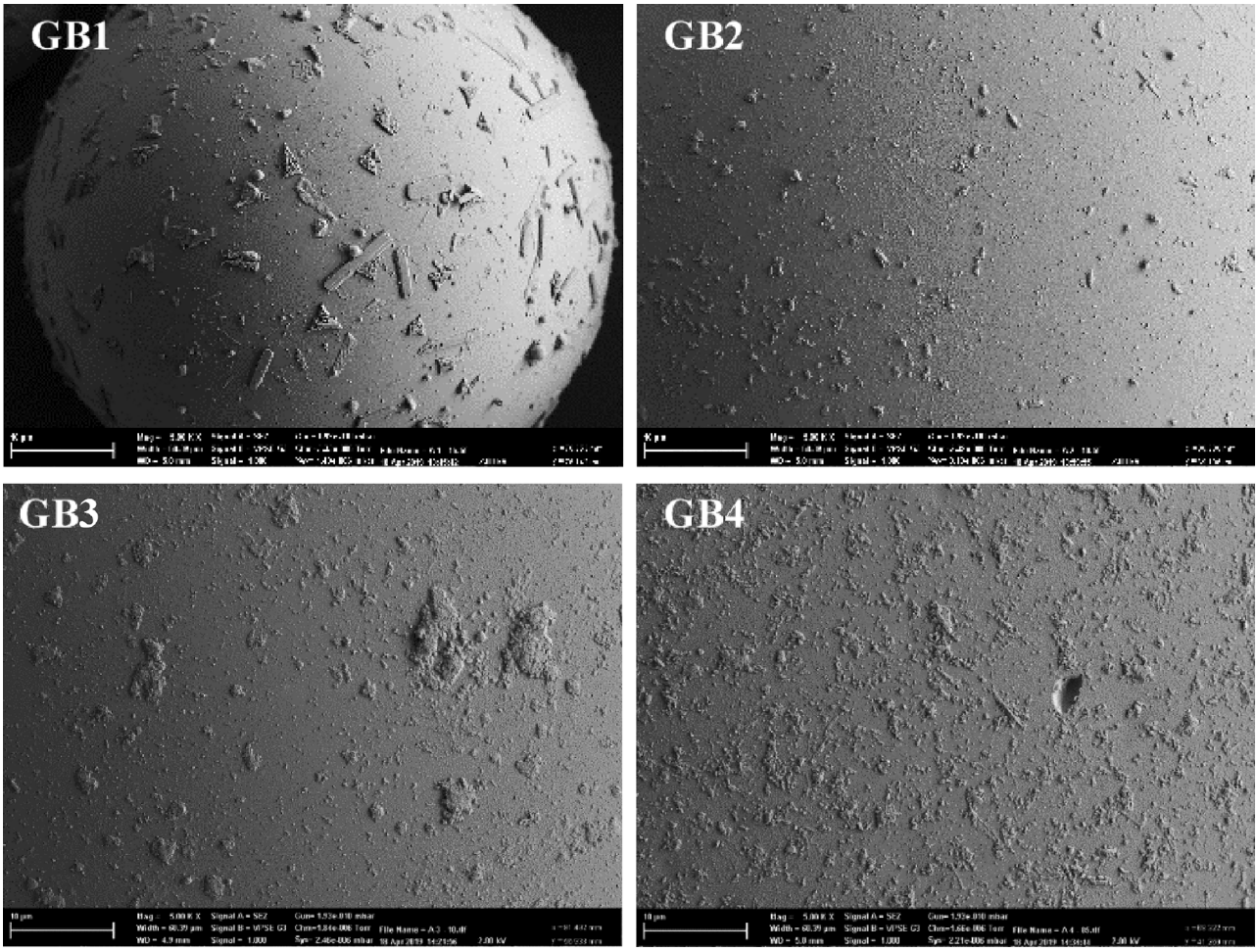

Fig. 8. SEM images of glass beads in different groups. [Scaled at 10 μm].

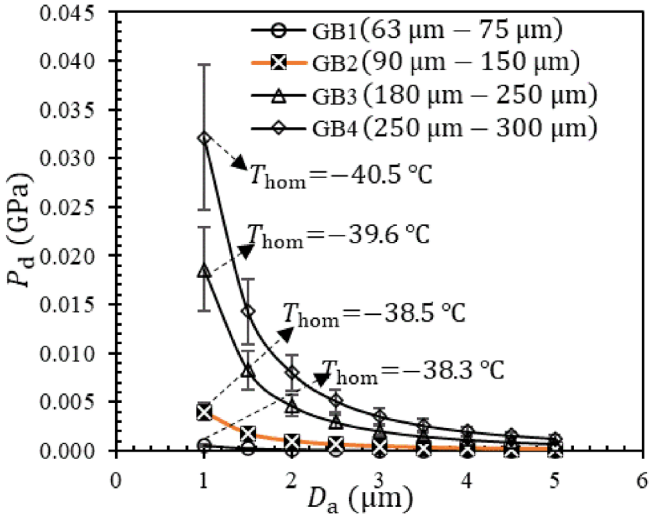

Fig. 9. Effect of the asperity equivalent diameter on P_d. [Vibration intensity: 0.0011 W/cm^2].

asperity involved in the collision. Moreover, D_a is estimated to be in the range of 1 μm – 10 μm from the analysis of SEM images. For D_a < 1 μm, the chance of contacting the substrate is negligible. The calculated P_d values are plotted in Fig. 9 against D_a. Clearly, P_d rises sharply as D_a reduces from 10 μm to 1 μm. Meanwhile, P_d is positively related to D_p. Thus the highest pressure, i.e., P_d = 0.032 GPa, occurs atD_a = 1 μm (D_p = GB4). At such a high pressure, according to Eq. (12), the corresponding homogeneous nucleation temperature is T_{hom} = −40.5 °C. Therefore, the ice nucleation cannot be triggered inside the water droplet for $T_o \geq -6.5$ °C. Moreover, GB4 has the densest asperities (Fig. 8) with the total contact area greatly increased, which may bring down the value of P_d to some extent. This might explain why f_{ice} of GB4 is less than that of GB3 in Fig. 7(b). Overall, it is clear that by direct collisions alone it is not sufficient to induce ice nucleation for $T_o \geq -6.5$ °C.

Given that the cavitation bubbles in the crevice are frequently exposed to the high pressure built up inside the water film, cavitation bubbles are highly likely to collapse and generate much higher local pressures.

To numerically investigate the dynamics of bubble collapse in the crevice, the range of P_d is chosen to be from 0.01 GPa to 0.08 GPa. Three simplified/representative crevice structures are investigated, namely, square-shape, cone-shape, and hemisphere-shape. The size of the crevice (i.e., radius, height, or width) is set to vary around 0.5 μm, corresponding to 125 lu. Conversions between lattice units and physical units are given in Table 3. In the present study, a computational domain of 401 × 401 grid (1.6 μm × 1.6 μm) is applied for the three crevice structures. The bottom half of the computational domain is set as fluid region where the initial density is artificially changed to obtain different P_d; the top half of the computational domain is set as solid region where the crevice inhabits, as exemplified in Fig. 10 with the hemisphere-shape crevice. The left and right boundaries of the computational domain are set as periodic boundary; the top and bottom boundaries are set as solid boundary.

Table 3
Unit conversion table.

Parameter	Lattice unit	Physics unit
Length	1	4.0×10^{-9} m
Time	1	1.6×10^{-12} s
Temperature	1	647.1 °C
Viscosity [a]	0.1	1.0×10^{-6} m^2/s
Density	0.1	0.247 g/cm^3
Pressure	0.1	848.5 MPa

[a] Values at 20 °C.

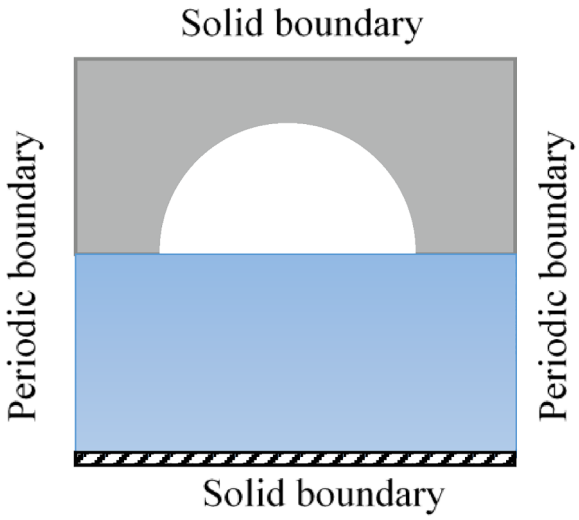

Fig. 10. Boundary conditions of the computational domain.

Fig. 11 shows the maximum collapse pressure (P_{max}) generated when a cavitation bubble collapses in the square-shape crevice for different crevice heights (H_{sq}) and widths (W_{sq}) with P_d = 0.08 GPa. As shown in Fig. 11(a), with W_{sq} fixed at 0.80 μm, P_{max} increases with increasing H_{sq}. When $H_{sq}$is fixed at 0.72 μm, P_{max} increases first as W_{sq}increases from 0.16 μm to 0.24 μm, and then drops with W_{sq}increases further to 0.48 μm, and increases again with W_{sq}becomes greater than 0.48 μm, as shown in Fig. 11(b). The first and second rises in P_{max} could be attributed to the primary and secondary bubble collapses, respectively. When $W_{sq}$is smaller than 0.24 μm, P_{max} is solely determined by the primary collapse. When $W_{sq}$is above 0.48 μm, there are two secondary bubbles formed after the primary collapse. Hence, the effect of W_{sq} is different in three regions: i: $W_{sq} \leq 0.24$ μm, the primary collapse is dominant; ii: 0.24 μm $< W_{sq} \leq$ 0.48 μm, transition stage; iii: 0.48 μm $< W_{sq}$, the secondary collapse is dominant. In the transition stage, the decrease in P_{max} can be attributed to the energy required to form secondary bubbles. The secondary bubble collapses under the high-pressure wave released from the primary collapse. Fig. 12 shows the pressure evolution from the primary collapse to the secondary collapse. The primary collapse is circled out by the red dashed line; the secondary collapse is circled out by the red solid line. The highest pressure generated by the cavitation bubble collapse in the square-shape crevice is P_{max} = 0.68 GPa, corresponding to a homogeneous ice nucleation temperature of $T_o \geq -3.4$ °C. Clearly, the ice nucleation inside the droplet cannot be triggered with such a low T_{hom}. Therefore, for $P_d \leq$ 0.08 GPa, the bubble collapse in the square-shape crevice cannot generate a pressure that is high enough to induce ice nucleation.

For cavitation bubble collapse in the cone-shape crevice with P_d = 0.08 GPa, the effects of crevice height (H_{co}) and radius (R_{co}) on P_{max} are plotted in Fig. 13. With R_{co}fixed at 0.8 μm, P_{max} increases with increasing H_{co}. This increase is primarily due to the increased cavitation bubble size. Oppositely, if $H_{co}$is fixed at 0.72 μm, P_{max} decreases with decreasing R_{co}. The highest pressure achieved in the cone-shape crevice is 0.89 GPa, corresponding to $T_{hom} \geq -20.7$ °C. This is a big leap in T_{hom} compared to the one from the square-shape crevice. However, considering the droplet temperature (i.e., $T_o \in (-9$ °C, 0 °C)) applied in the experiment, 0.89 GPa is still not enough for triggering the ice nucleation. Consequently, for $P_d \leq$ 0.08 GPa, ice nucleation cannot be triggered by the bubble collapse in the cone-shape crevice. Fig. 14 shows the pressure distribution of a typical cavitation bubble collapse in a cone-shape crevice. Due to the presence of the conical surface, the driving pressure is guided toward the left and right sides of the bubble, forming two high pressure regions as circled out by a red solid line as shown in Fig. 14. Thus, the occurrence of secondary bubble collapses could be prohibited. Without the energy consumed by the formation of secondary bubbles, the primary collapse in the cone-shape crevice could achieve a relatively higher collapse pressure than in the square-shape.

Fig. 15 shows the maximum collapse pressure of cavitation bubbles in the hemisphere-shape crevice. For $P_d >$ 0.05 GPa, the present model becomes unstable due to the supersonic current generated in the

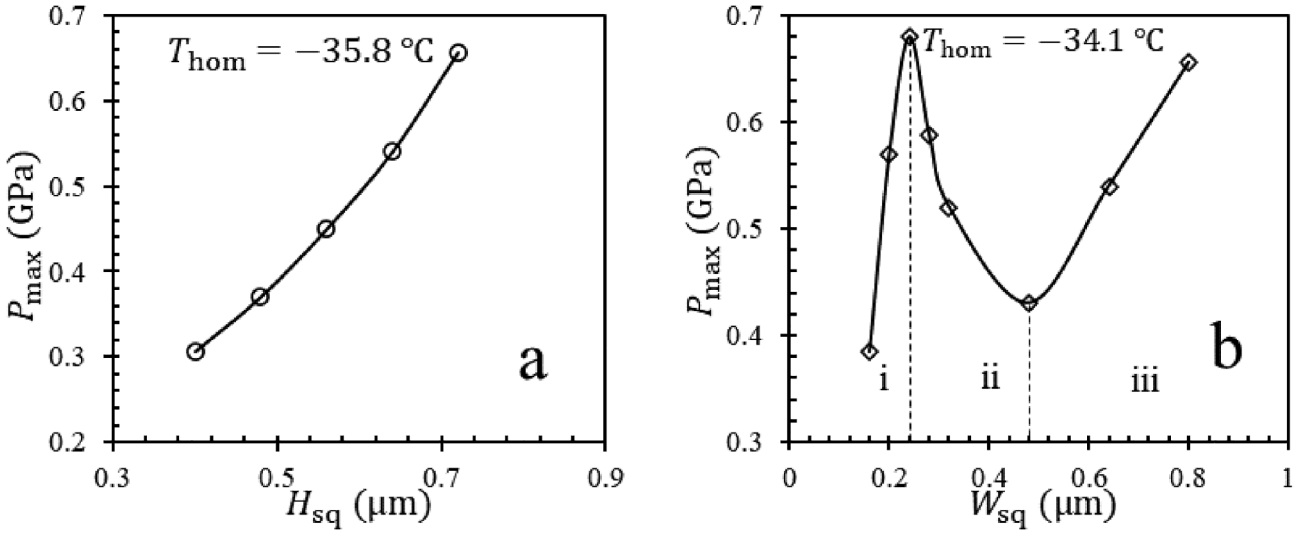

Fig. 11. Effects of height and width of the square-shape crevice on P_{max} at P_d = 0.08 GPa. (a) crevice height effect on P_{max} with width fixed at 0.80 μm; (b) crevice width effect on P_{max} with height fixed at 0.64 μm [i: primary collapse dominant; ii: transition from primary collapse dominant to secondary collapse dominant; iii: secondary collapse dominant].

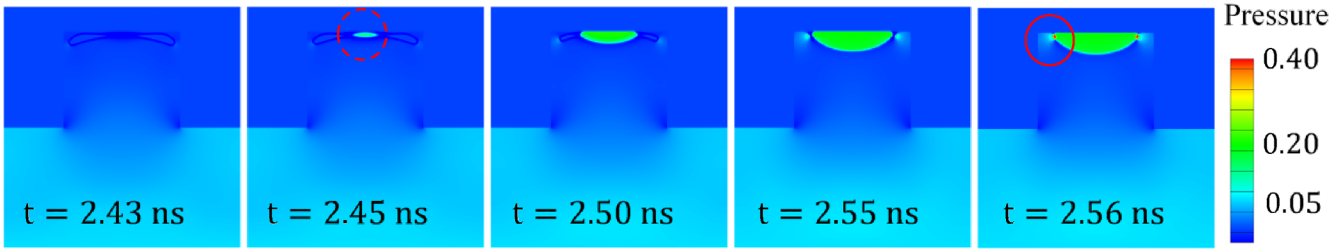

Fig. 12. Pressure field of the cavitation bubble collapse in the square-shape crevice. The primary collapse is circled out by the red dashed line; the secondary collapse is circled out by the red solid line. [H_{sq}: 0.64 μm, W_{sq}: 0.8 μm; pressure unit: GPa].

collapse is beyond the capability of the present model. Therefore, P_d is reduced to 0.05 GPa to ensure numerical stability. As shown in Fig. 15(a), P_{max} is found positively related to R_{he} with P_d fixed at 0.05 GPa. When R_{he} reaches 0.4 μm, the collapse pressure achieves its peak of P_{max} = 1.63 GPa, corresponding to an ice nucleation temperature of T_{hom} = 12.7 °C. This T_{hom} is theoretically high enough to induce ice nucleation in the water droplet for $T_o \in (-9\ °C, 0\ °C)$. With R_{he} fixed at 0.4 μm, the effect of P_d on P_{max} is investigated and the result is plotted in Fig. 15(b). The distance between the final position of the cavitation bubble and the bottom boundary is also recorded and denoted as Y_p. The final position is defined as the centre of the cavitation bubble in the last phase of collapse. With increasing P_d from 0.01 GPa to 0.016 GPa, P_{max} rises sharply from 1.26 GPa to 1.56 GPa then gradually drops from 1.56 GPa to 1.39 GPa with P_d increases from 0.016 GPa to 0.039 GPa. Finally, P_{max} rises again from 1.39 GPa to 1.63 GPa. The decrease in P_{max} for $P_d \in$ (0.016 GPa, 0.039 GPa) is attributed to the reduction in Y_p. As can be seen in Fig. 15(b), Y_p decreases with increasing P_d. When Y_p reaches below 0.495 μm, the bubble moves into the region where the local pressure is significantly reduced by the solid boundary [57,58]. Therefore, the pressure difference across the bubble interface is greatly reduced. With further decreasing Y_p, the local pressure near the solid boundary becomes stable. Therefore, when $P_d \geq$ 0.039 GPa, P_{max} starts rising again. For P_d = 0.01 GPa, the obtained P_{max} is 1.26 GPa, corresponding to T_{hom} = −2.1 °C which is still high enough to induce ice nucleation. Considering the pressure range of P_d in Fig. 9, it can be concluded that bubble collapse in the hemisphere-shape crevice generates a pressure high enough for triggering ice nucleation inside the water droplet.

Fig. 16 shows the pressure evolution before and after the cavitation bubble collapse at t = 2.109 ns in a hemisphere-shape crevice. Compared to the square-shape and cone-shape crevices, the bubble collapse in the hemisphere-shape crevice generates a relatively higher collapse pressure. Considering the different crevice structures, the cavitation bubbles in the hemisphere-shape crevice has a much less contact area with the solid boundary during collapse. As circled out by the red solid line in Fig. 16, in the final stage of the bubble collapse, the bubble is entirely separated from the solid boundary. The presence of solid boundary leads to the formation of a low-pressure region and breaks the symmetry of external pressure distribution around the bubble [57]. Consequently, cavitation bubbles in the hemisphere-shape crevice tend to have a higher pressure jump across the bubble interface than in the other two crevices.

Based on the above discussion on cavitation bubble dynamics in crevices, a conclusion can be reached that the collapse of cavitation bubbles in the crevice is structure sensitive. Not all cavitation bubble collapses in the crevice can induce ice nucleation and the bubble collapse in the hemisphere-shape crevice proves capable of generating a pressure that is high enough for triggering ice nucleation in the water droplet. In addition, the above simulations are run for cases with a single asperity. Given the dense asperities at the particle surface, the number of asperities involved in the collision between the particle and the vibrating substrate should be way greater than one, leading to the dramatic increase in the contact area. As a consequence, P_d might be significantly reduced. This could be confirmed by the experimental result shown in Fig. 7(a) where the case with single particle has no ice nucleation. When two or more particles are contained in the droplet, the momentum transferred between each other could remarkably increase P_d. Also, though not captured by the high-speed camera in the experiments of this study, the microstreaming (or flow streams) caused by the oscillating cavitation bubbles could also contribute to (or even solely induce) the initialisation of ice nucleation [19,29,54]. Significant further work, albeit a valuable next step, is required to confirm and elucidate the contribution from bubble oscillation, which exceeds much beyond the scope of the current effort.

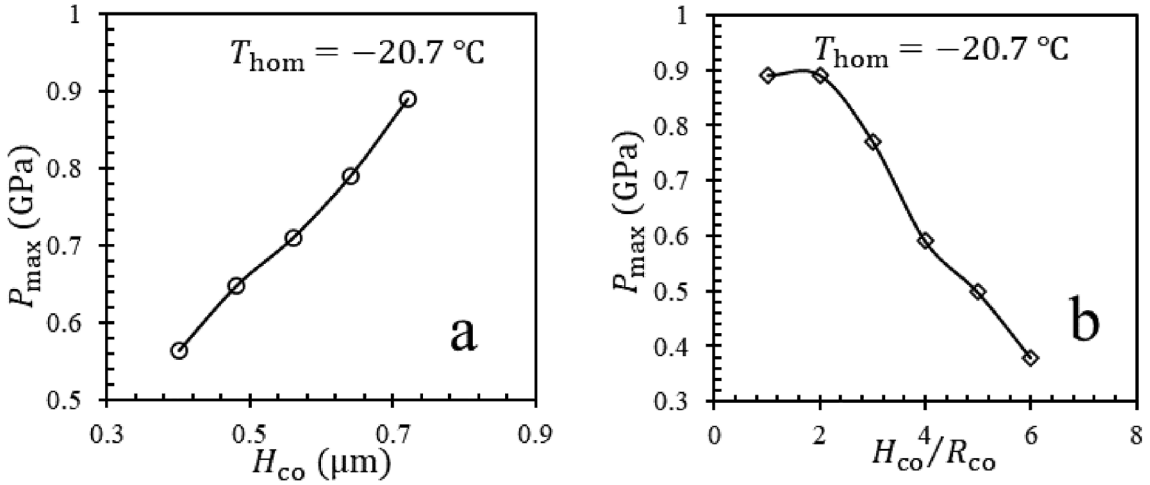

Fig. 13. Collapse of cavitation bubbles in the cone-shape crevice at P_d = 0.08 GPa. (a) effect of the crevice height on P_{max} with width fixed at 0.8 μm; (b) effect of the crevice radius on P_{max} with height fixed at 0.72 μm.

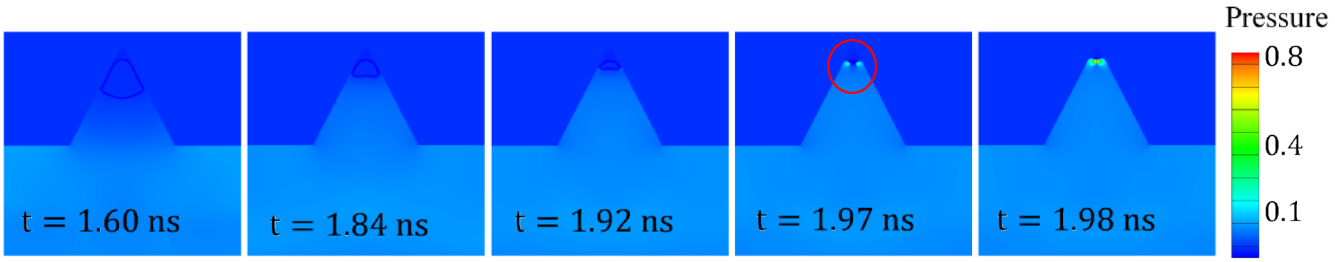

Fig. 14. Pressure field of the cavitation collapse in the cone-shape crevice. [R_{co}: 0.4 μm; H_{co}: 0.72 μm; pressure unit: GPa].

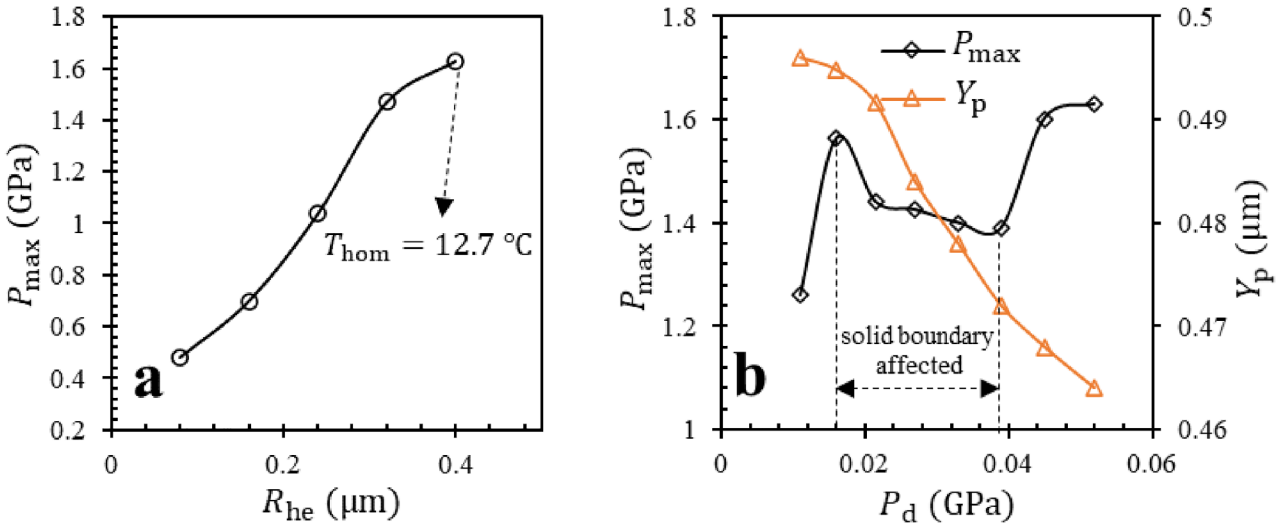

Fig. 15. Maximum collapse pressure of cavitation bubbles in the hemisphere-shape crevice. (a) effect of the crevice radius on P_{max} at P_d = 0.05 GPa; (b) effect of P_d on P_{max} with crevice radius fixed at 0.4 μm.

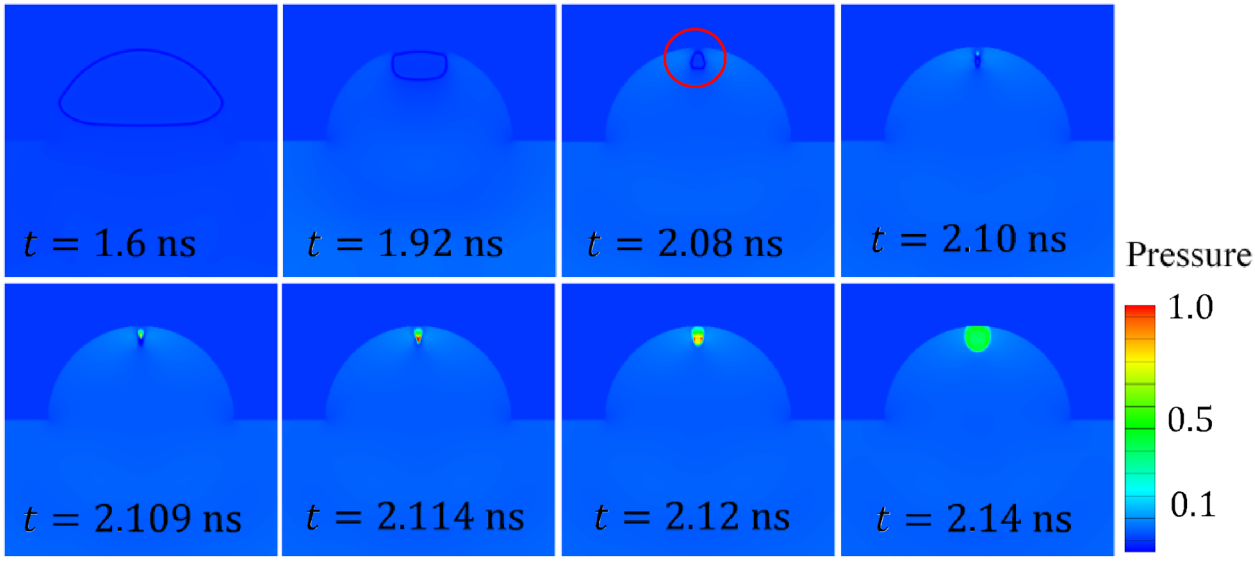

Fig. 16. Pressure field of the cavitation collapse in the hemisphere-shape crevice. [R_{he}: 0.4 μm; pressure unit: GPa].

5. Conclusion

In this study, ice nucleation of water droplets containing glass bead particles in the field of weak ultrasonic vibration was experimentally investigated. Numerical simulations based on LBM were conducted to examine the cavitation bubbles dynamics in the crevices at the particle surface.

Ice nucleation was induced by weak ultrasonic vibrations with the assistance of particles at relatively high temperatures (up to −2 ˚C). The nucleation sites were only observed in the region between the particle and the substrate. For water droplets with only one particle, the ice nucleation could not be initiated. When the particle number concentration was increased to 2 − 3 particles/droplet, the fraction of frozen droplets (f_{ice}) increased to 5.6% at the temperature of −3.5 ˚C. f_{ice}

increased as the particle number concentration increased, or as the droplet initial temperature decreased. The particle size also played an important role in determining f_{ice}, particularly at low temperatures. The peaks of f_{ice} were constantly found when using particles with diameters of 180 − 250 μm at the vibration intensity of 0.0011 W/cm^2.

The maximum collision pressure (P_d) generated in the particle–substrate collision was estimated to be less than 0.04 GPa which was insufficient for triggering ice nucleation. The collapse of cavitation bubbles in the crevice, on the other hand, generated the extremely high point pressure required for ice nucleation. The collapse of cavitation bubbles in the crevice is structure sensitive. Compared to those in square-shape and cone-shape crevices, the bubble collapse only in the hemisphere-shape crevice generated pressures that are high enough to induce ice nucleation inside water droplets due to the lower contact area with the solid boundary. Microstreaming caused by bubble oscillation could also play a significant role in triggering ice nucleation. Significant work is required to elucidate the fundamental physics underlying the initialisation of ice nucleation under the combined effects of the presence of glass bead particles and the external field of ultrasonic vibration.

CRediT authorship contribution statement

Shaolei Gai: Conceptualization, Software, Investigation, Formal analysis, Writing - review & editing. **Zhengbiao Peng:** Supervision, Conceptualization, Writing - review & editing. **Behdad Moghtaderi:** Supervision. **Jianglong Yu:** Supervision. **Elham Doroodchi:** Supervision, Conceptualization, Writing - review & editing, Project administration.

Declaration of Competing Interest

The authors declare that they have no known competing financial interests or personal relationships that could have appeared to influence the work reported in this paper.

Acknowledgement

The authors wish to acknowledge the financial support by Australian Research Council (ARC) (Project ID: G1900137).

Appendix A. Supplementary data

Supplementary data to this article can be found online at https://doi.org/10.1016/j.ultsonch.2020.105301.

References

[1] P. Zhang, Z.W. Ma, An overview of fundamental studies and applications of phase change material slurries to secondary loop refrigeration and air conditioning systems, Renew. Sustain. Energy Rev. 16 (2012) 5021–5058.
[2] M. Kauffeld, M.J. Wang, V. Goldstein, K.E. Kasza, Ice slurry applications, Int. J. Refrig. 33 (2010) 1491–1505.
[3] Z. Peng, Z. Yuan, K. Liang, J. Cai, Ice slurry formation in a cocurrent liquid-liquid flow, Chin. J. Chem. Eng. 16 (2008) 552–557.
[4] T. Asaoka, A. Saito, S. Okawa, H. Kumano, T. Hozumi, Vacuum freezing type ice slurry production using ethanol solution 2nd report: Investigation on evaporation characteristics of ice slurry in ice production, Int. J. Refrig. 32 (2009) 394–401.
[5] T. Asaoka, A. Saito, S. Okawa, T. Ito, N. Izumi, Vacuum freezing type ice slurry production using ethanol solution 1st report: Measurement of vapor–liquid equilibrium data of ethanol solution at 20 °C and at the freezing temperature, Int. J. Refrig. 32 (2009) 387–393.
[6] Robert G. Dorsch, P.T. Hacker, Photomicrographic investigation of spontaneous freezing temperature of supercooled water droplets, in: National advisory committe for aeronautics, 1950.
[7] E.A. Svensson, C. Delval, P.V. Hessberg, M.S. Johnson, J. Pettersson, Freezing of water droplets colliding with kaolinite particles, Atmos. Chem. Phys. 9 (2009) 4295–4300.
[8] G. Fraux, J.P.K. Doye, Note: Heterogeneous ice nucleation on silver-iodide-like surfaces, J. Chem. Phys. 141 (2014) 216101.
[9] V.D. Aleksandrov, A.A. Barannikov, N.V. Dobritsa, Effect of magnetic field on the supercooling of water drops, Inorg. Mater. 36 (2000) 895–898.
[10] X.-X. Zhang, X.-H. Li, M. Chen, Role of the electric double layer in the ice nucleation of water droplets under an electric field, Atmos. Res. 178–179 (2016) 150–154.
[11] D. Rzesanke, J. Nadolny, D. Duft, R. Muller, A. Kiselev, T. Leisner, On the role of surface charges for homogeneous freezing of supercooled water microdroplets, PCCP 14 (2012) 9359–9363.
[12] P. Gao, B. Cheng, X. Zhou, D. Zhang, G. Zhou, Study on droplet freezing characteristic by ultrasonic, Heat Mass Transf. 53 (2017) 1725–1734.
[13] M. Dalvi-Isfahan, N. Hamdami, E. Xanthakis, A. Le-Bail, Review on the control of ice nucleation by ultrasound waves, electric and magnetic fields, J. Food Eng. 195 (2017) 222–234.
[14] B. Wang, A. Laskin, T. Roedel, M.K. Gilles, R.C. Moffet, A.V. Tivanski, D.A. Knopf, Heterogeneous ice nucleation and water uptake by field-collected atmospheric particles below 273 K, Journal of Geophysical Research: Atmospheres, 117 (2012) n/a-n/a.
[15] B.J. Murray, D. O'Sullivan, J.D. Atkinson, M.E. Webb, Ice nucleation by particles immersed in supercooled cloud droplets, Chem. Soc. Rev. 41 (2012) 6519–6554.
[16] F. Lüönd, O. Stetzer, A. Welti, U. Lohmann, Experimental study on the ice nucleation ability of size-selected kaolinite particles in the immersion mode, Journal of Geophysical Research: Atmospheres, 115 (2010) n/a-n/a.
[17] C.A. Stan, G.F. Schneider, S.S. Shevkoplyas, M. Hashimoto, M. Ibanescu, B.J. Wiley, G.M. Whitesides, A microfluidic apparatus for the study of ice nucleation in supercooled water drops, Lab Chip 9 (2009) 2293–2305.
[18] C.F. Cooper, W.C. Jolly, Ecological effects of silver iodide and other weather modification agents: a review, Water Resour. Res. 6 (1970) 88–98.
[19] H. Kiani, Z. Zhang, A. Delgado, D.-W. Sun, Ultrasound assisted nucleation of some liquid and solid model foods during freezing, Food Res. Int. 44 (2011) 2915–2921.
[20] R. Hickling, Nucleation of freezing by cavity collapse and its relation to cavitation damage, Nature 206 (1965) 915–917.
[21] R. Hickling, Nucleation of freezing by cavitation in sub-cooled bismuth and gallium, Nature 207 (1965) 742.
[22] R. Hickling, Transient, high-pressure solidification associated with cavitation in water, Phys. Rev. Lett. 73 (1994) 2853–2856.
[23] X. Zhang, T. Inada, A. Yabe, S. Lu, Y. Kozawa, Active control of phase change from supercooled water to ice by ultrasonic vibration 2. Generation of ice slurries and effect of bubble nuclei, Int. J. Heat Mass Transf. 44 (2001) 4533–4539.
[24] C. Virone, H.J.M. Kramer, G.M. van Rosmalen, A.H. Stoop, T.W. Bakker, Primary nucleation induced by ultrasonic cavitation, J. Cryst. Growth 294 (2006) 9–15.
[25] M. Saclier, R. Peczalski, J. Andrieu, A theoretical model for ice primary nucleation induced by acoustic cavitation, Ultrason. Sonochem. 17 (2010) 98–105.
[26] D. Yu, B. Liu, B. Wang, The effect of ultrasonic waves on the nucleation of pure water and degassed water, Ultrason. Sonochem. 19 (2012) 459–463.
[27] R. Chow, R. Blindt, R. Chivers, M. Povey, The sonocrystallisation of ice in sucrose solutions: primary and secondary nucleation, Ultrasonics 41 (2003) 595–604.
[28] R. Chow, R. Blindt, R. Chivers, M. Povey, A study on the primary and secondary nucleation of ice by power ultrasound, Ultrasonics 43 (2005) 227–230.
[29] R. Chow, R. Blindt, A. Kamp, P. Grocutt, R. Chivers, The microscopic visualisation of the sonocrystallisation of ice using a novel ultrasonic cold stage, Ultrason. Sonochem. 11 (2004) 245–250.
[30] X. Zhang, T. Inada, A. Tezuka, Ultrasonic-induced nucleation of ice in water containing air bubbles, Ultrason. Sonochem. 10 (2003) 71–76.
[31] J. Dodds, F. Espitalier, O. Louisnard, R. Grossier, R. David, M. Hassoun, F. Baillon, C. Gatumel, N. Lyczko, The effect of ultrasound on crystallisation-precipitation processes: some examples and a new segregation model, Part. Part. Syst. Char. 24 (2007) 18–28.
[32] O. Louisnard, F.J. Gomez, R. Grossier, Segregation of a liquid mixture by a radially oscillating bubble, J. Fluid Mech. 577 (2007) 385–415.
[33] C. Marcolli, Ice nucleation triggered by negative pressure, Sci. Rep. 7 (2017) 16634.
[34] J.D. Hunt, K.A. Jackson, Nucleation of the solid phase by cavitation in an undercooled liquid which expands on freezing, Nature 211 (1966) 1080–1081.
[35] M. Patrick, R. Blindt, J. Janssen, The effect of ultrasonic intensity on the crystal structure of palm oil, Ultrason. Sonochem. 11 (2004) 251–255.
[36] F. Caupin, E. Herbert, Cavitation in water: a review, C.R. Phys. 7 (2006) 1000–1017.
[37] B. Vukasinovic, M.K. Smith, A.R.I. Glezer, Dynamics of a sessile drop in forced vibration, J. Fluid Mech. 587 (2007) 395–423.
[38] Z. Peng, Y.A. Alghamdi, B. Moghtaderi, E. Doroodchi, CFD-DEM investigation of transition from segregation to mixing of binary solids in gas fluidised beds, Adv. Powder Technol. 27 (2016) 2342–2353.
[39] Z. Peng, S.V. Ghatage, E. Doroodchi, J.B. Joshi, G.M. Evans, B. Moghtaderi, Forces acting on a single introduced particle in a solid–liquid fluidised bed, Chem. Eng. Sci. 116 (2014) 49–70.
[40] Y. Yang, M. Shan, X. Kan, Y. Shangguan, Q. Han, Thermodynamic of collapsing cavitation bubble investigated by pseudopotential and thermal MRT-LBM, Ultrason. Sonochem. 62 (2020) 104873.
[41] S. Gai, Z. Peng, B. Moghtaderi, J. Yu, E. Doroodchi, LBM modelling of supercooled water freezing with inclusion of the recalescence stage, Int. J. Heat Mass Transf. 146 (2020) 118839.
[42] L. Guan, Z. Yuan, B. Moghtaderi, Z. Peng, G.M. Evans, C. Gu, E. Doroodchi, Prediction of terminal velocity of fractal aggregates with IBM-LBM method, Powder Technol. 361 (2020) 1060–1069.
[43] A. Olmo, R. Baena, R. Risco, Use of a droplet nucleation analyzer in the study of water freezing kinetics under the influence of ultrasound waves, Int. J. Refrig. 31 (2008) 262–269.
[44] B.M. Borkent, M. Arora, C.-D. Ohl, N. De Jong, M. Versluis, D. Lohse, K.A. MØRch, E. Klaseboer, B.C. Khoo, The acceleration of solid particles subjected to cavitation

nucleation, J. Fluid Mech. 610 (2008) 157–182.
[45] M. Arora, C.-D. Ohl, K.A. Mørch, Cavitation inception on microparticles: a self-propelled particle accelerator, Phys. Rev. Lett. 92 (2004) 174501.
[46] T.J. Matula, Inertial cavitation and single–bubble sonoluminescence, Philos. Trans. R. Soc. Lon. Ser. A Mathemat. Phys. Eng. Sci. 357 (1999) 225.
[47] Q. Li, K.H. Luo, X.J. Li, Forcing scheme in pseudopotential lattice Boltzmann model for multiphase flows, Phys. Rev. E 86 (2012) 016709.
[48] C. Peng, S. Tian, G. Li, M.C. Sukop, Single-component multiphase lattice Boltzmann simulation of free bubble and crevice heterogeneous cavitation nucleation, Phys. Rev. E 98 (2018) 023305.
[49] M. Choukroun, O. Grasset, Thermodynamic model for water and high-pressure ices up to 2.2GPa and down to the metastable domain, J. Chem. Phys. 127 (2007) 124506.
[50] T. Inada, X. Zhang, A. Yabe, Y. Kozawa, Active control of phase change from supercooled water to ice by ultrasonic vibration 1. Control of freezing temperature, Int. J. Heat Mass Transf. 44 (2001) 4523–4531.
[51] J. Sun, J. Gong, G. Li, A lattice Boltzmann model for solidification of water droplet on cold flat plate, Int. J. Refrig 59 (2015) 53–64.
[52] Z. Guo, B. Shi, C. Zheng, A coupled lattice BGK model for the Boussinesq equations, Int. J. Numer. Meth. Fluids 39 (2002) 325–342.
[53] X. Chen, Simulation of 2D cavitation bubble growth under shear flow by lattice Boltzmann model, J Commun. Comput. Phys. 7 (2010) 212.
[54] F. Hu, D.-W. Sun, W. Gao, Z. Zhang, X. Zeng, Z. Han, Effects of pre-existing bubbles on ice nucleation and crystallization during ultrasound-assisted freezing of water and sucrose solution, Innovat. Food Sci. Emerg. Technol. 20 (2013) 161–166.
[55] L. Zheng, D.-W. Sun, Innovative applications of power ultrasound during food freezing processes—a review, Trends Food Sci. Technol. 17 (2006) 16–23.
[56] S. Gai, Z. Peng, B. Moghtaderi, J. Yu, E. Doroodchi, Effect of ultrasonic vibration on the nucleation onset of temperature of micro-sized water droplets, in: Chemeca 2018, Queenstown, NZ, 2018, pp. 234.
[57] C. Peng, S. Tian, G. Li, M.C. Sukop, Simulation of laser-produced single cavitation bubbles with hybrid thermal Lattice Boltzmann method, Int. J. Heat Mass Transf. 149 (2020) 119136.
[58] A. Philipp, W. Lauterborn, Cavitation erosion by single laser-produced bubbles, J. Fluid Mech. 361 (1998) 75–116.